Plasma Density Measurements of the Inner Shell Release

D. Haberberger, A. Shvydky, V. N. Goncharov, D. Cao, J. Carroll-Nellenback, S. X. Hu, S. T. Ivancic, V. V. Karaseiv, J. P. Knauer, A. V. Maximov, and D. H. Froula

Phys. Rev. Lett. **123**, 235001 — Published 2 December 2019

DOI: 10.1103/PhysRevLett.123.235001

Version 1.0 as of October 28, 2019
To be submitted to PRL

Plasma Density Measurements of the Inner Shell Release

D. Haberberger,[1,*] A. Shvydky,[1] V. N. Goncharov,[1] D. Cao,[1] J. Carroll-Nellenback,[1] S. X. Hu,[1] S. T. Ivancic,[1] V. V. Karaseiv,[1] J. P. Knauer,[1] A. V. Maximov,[1] and D. H. Froula[1]

[1]*Laboratory for Laser Energetics, University of Rochester, Rochester, New York 14623, USA*

(Dated: October 28, 2019)

The material release on the side opposite to the laser drive of a CH shell was probed at conditions relevant to inertial confinement fusion (ICF). The release was found to expand further with a longer scale length than that predicted by radiation-hydrodynamic simulations. The simulations show that a relaxation of the back side of the shell consistent with measurements explains the experimentally observed reduction in ICF implosion performance—specifically, reduced areal density at peak compression.

PACS numbers:

While great progress has been made over recent years in inertial confinement fusion (ICF) experiments [2], achieving ignition conditions remains a grand challenge. In both direct- and indirect-drive approaches to fusion, a cold layer of deuterium–tritium (DT) fuel is compressed by material ablation to form a high-areal-density confinement around an igniting central hot spot. In both approaches, several shocks are launched through the outer solid-density DT fuel and into a central DT vapor region. Once the shocks break through the inner surface into the central region, the fuel spherically converges to form a high-areal-density confinement. By limiting the amount of material released into the central region and maintaining a low temperature inside the vapor region before stagnation, the implosion can reach maximum convergence and the hot-spot temperatures necessary for ignition.

One of the reasons for the underperformance in the recent experiments is attributed to a reduced areal density of the fuel: a 20% deficiency has been reported for most of the implosions on the National Ignition Facility [1]. Several mechanisms could contribute to the reduction in shell convergence, and therefore in areal density, including mixing of the ablator material into the fuel through a premature release of material from the inner surface or mixing of the fuel into the central hot spot. In addition, inaccurate modeling of material preheat (x-rays or fast electrons) or the material properties of the fuel interacting with multiple strong shocks both could lead to an underprediction of the material release from the inner surface of the main shell by material release after the shock breaks through the shell. Such a release is created as the first shock breaks out of the main fuel into the vapor region of the target. The rate of the expansion of this material into the inner shell is determined by several factors, including sound speed, ion viscosity, and thermal conduction.

Experimental signatures of the driven shell dynamics are commonly used to test hydrodynamic simulations. In implosion experiments, x-ray backlighting or self-emission measurements are used to track the shell trajectory [3] but give no information about the material release behind the shell since the low-density material does not attenuate the high-energy x-ray photons. Optical probing with a velocity interferometer system for any reflector (VISAR) is used to track a shock moving through a transparent material or to measure when the shock breaks out into vacuum [4]. Although these measurements are very useful for studying equation of state (EOS) used in simulation codes, no information is gained about the profile of material release when the shock breaks through the shell because at this point the optical beam is absorbed near the critical plasma density.

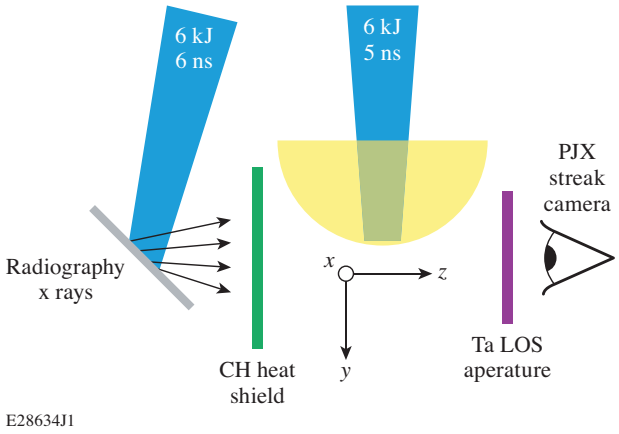

FIG. 1: The experimental setup used four UV lasers (blue): two beams incident upon an aluminum foil target (gray) for creating the x-ray backlighter and two beams to drive the CH shell (yellow). A tantalum foil (purple) with a 100-μm slit oriented in the $\hat{y}$ direction was used to prevent integration over the $\hat{x}$ direction by the streak camera. The 4ω probe laser (not shown for clarity) passed through the interaction region at a 30° angle to the negative $\hat{z}$ axis in the $\hat{x}$–$\hat{z}$ plane.

In this Letter, we present the first direct measurements

of the low-density plasma released from the rear side of a laser-driven shell. The low-density plasma (at 10^{20} cm^{-3}) was measured to travel ∼190 μm ahead of the driven shell with a scale length that increased to a maximum of 63 μm over 3 ns. These observations are in contrast to hydrodynamic simulations that show the plasma traveling ∼80 μm away from the shell with a density gradient that increased to 15 μm. Further investigation uncovered the sensitivity of the rear shell expansion to the initial (pre-shock breakout) CH density profile. By initiating the back side of the shell with a 10-μm density gradient, release profiles matching those observed in the experiment were obtained in the simulations. The more rapid expansion results from shock heating of the lower density material as it breaks out, causing a higher sound speed, and therefore a faster post-shock expansion. Implementing an expanded profile on the back side of the DT ice layer in ICF implosion simulations shows a significant decrease in both the areal density and neutron yield.

The experiments were carried out on the OMEGA EP Laser System [5]. A 37-μm-thick, 4-mm-diam hemispherical CH shell (used to prevent parallax in line-integrated diagnostics) was irradiated from the inner side by two ultraviolet (UV) lasers with a central wavelength of λ = 351 nm (Fig. 1). With a combined laser energy of 6 kJ in a 5-ns square pulse, an overlapped intensity of 2.5 × 10^{14} W/cm^2 was obtained in a 750-μm-diam eighth-order super-Gaussian spot that was created using SG 8-0750 OMEGA EP distributed phase plates (DPP's). The laser-irradiated side is referred to as the "front" side and the side opposite the laser is referred to as the "rear" side.

The shell trajectory was tracked using x-ray radiography driven by the two other UV beams. Their overlapped intensity on the Al foil (6×10^{13} W/cm^2) was generated by a combined energy of 6 kJ in a 6-ns square pulse focused to a 750-μm-diam spot defined by the DPP's. The Al He$_\alpha$ x-rays (1.5 keV) propagated through the interaction region in the $\hat{z}$ direction and were recorded by an x-ray streak camera (PJXI), which imaged along the $\hat{y}$ direction. A 25-μm thick CH foil was used to filter out low-energy radiation from interfering with the interaction. Testing this configuration by probing at early times before the shock breaks out showed no expansion of the rear surface of the CH shell.

Figure 2(a) shows a radiograph where the shock is observed breaking out of the rear side at t = 580 ± 40 ps. After this time, the shell was observed to undergo a near-constant acceleration of ∼32 μm/ns^2 across ∼540 μm over 4 ns. For this experimental setup, the 1.5-keV x-rays provided an optimal peak absorption of ∼70%. The PJXI diagnostic had a measured spatial resolution of 20 μm, which was sufficient to track the position of the shell, although not small enough to resolve the expected shell thickness of 5 to 7 μm.

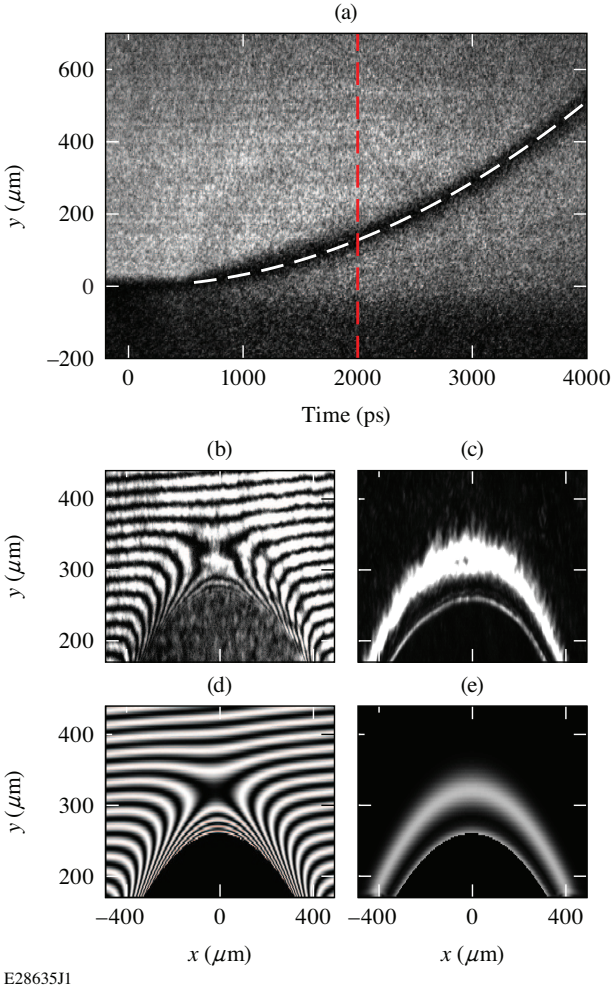

FIG. 2: (a) The PJXI diagnostic measured the shell trajectory by tracking the absorption of the Al He$_\alpha$ x-rays traveling through the interaction region. The origins of the spatial and temporal axes represent the initial location of the center of the CH shell (spatial) at the beginning of the drive laser pulse (2% of rise, temporal). The shell trajectory was fit with a constant acceleration of 32 μm/ns^2 (white dashed line). The 4ω probe diagnostic measures the density of the released plasma on the rear side of the driven shell through (b) interferometry and (c) AFR at 2 ns after the drive [timing shown by red dashed line in (a)]. The synthesized response of the (d) interferometry and (e) AFR diagnostics that best match the corresponding measurements at 2 ns. The origin of the $\hat{y}$ axis corresponds to the original location of the center of the CH shell.

To measure the density profile in the rarefaction wave, an 8-ps FWHM duration 4ω (263-nm) probe beam was used to generate interferometry [6] [Fig. 2(b)] and angular filter refractometry [7] [AFR, Fig. 2(c)] data. Its short duration ensured that there was inappreciable hydrodynamic movement over the measurement time. The fastest hydrodynamic expansion within the region of interest was ∼0.22 μm/ps, resulting in a maximum of 2 μm of spatial smearing over the 8-ps measurement. The interferometer used a Walloston prism to split the probe

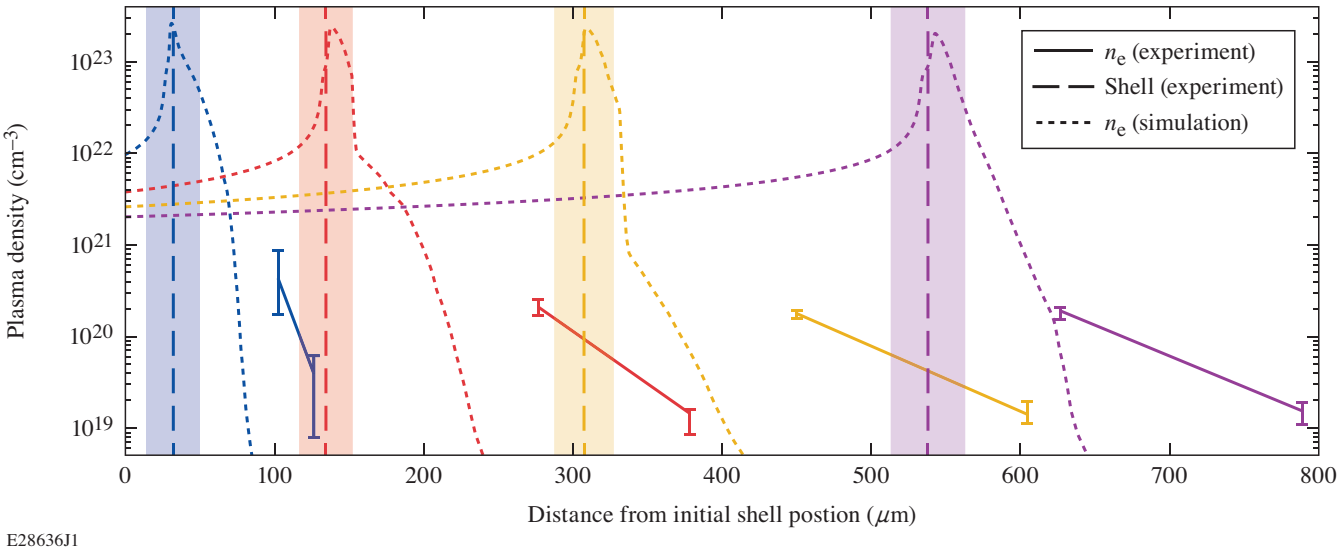

FIG. 3: The measured (solid curves) and simulated (dotted curves) plasma density profiles at 1 ns (blue), 2 ns (red), 3 ns (yellow), and 4 ns (purple) are plotted. The vertical dashed lines are the peak shell positions as measured by the PJXI diagnostic (with error bars shown by the shaded regions).

beam and overlap the two halves to form an interferogram that was used to extract the phase imparted on the beam as it propagated through the plasma, a signal proportional to the line-integrated plasma density (for more detail see [6]). The AFR used angular filters in a bullseye shape in the Fourier plane of the probe beam to block or transmit certain refraction angles of the light. Upon returning to the image plane, this results in light and dark bands that represent contours of constant refraction, a signal proportional the spatial derivative of the phase or line-integrated plasma density (for more detail see [7]). The two diagnostics were used in conjunction to gain confidence in the measured plasma density profiles.

The interaction was probed at four times with respect to the beginning of the drive beams (2% of rise): 1, 2 (Fig. 2), 3, and 4 ns. For the probe timing of 2 ns, the shell moved ~120 μm at the center of the laser spot [Fig. 2(a)]. Figure 2(b) shows the phase change accrued from propagating through the released plasma. A measurable phase change at the center of the shell is evident for distances greater than ~290 μm - for positions less than this the light was refracted outside of the collection optics. Refraction of the probe light from its propagation through this plasma resulted in the observation of two bands [Fig. 2(c)] of constant refraction angle corresponding to 0.75° (outer) and 3° (inner). The images were analyzed by simulating a synthetic interferogram and AFR image using an analytic function for the plasma density and iterating until the images converged. A single exponentially decaying profile in the $\hat{y}$ direction, with a Gaussian function in the $\hat{x}$ and $\hat{z}$ directions, was found to be adequate to reproduce the measurements. Other analytic profiles were tested and delivered very similar results. The matched synthetic interferogram and AFR image for the 2 ns data are shown in Figs. 2(d) and 2(e), respectively, and correspond to a plasma density profile of $n_e(x,y,z) = n_o \exp[-y/L_y]\exp\{-(x^2+z^2)/[L_{FWHM}/2\ln(2)]\}$, where $n_o = 3.6\times10^{21}$ cm^{-3}, $L_y = 38$ μm, and $L_{FWHM} = 340$ μm. Note, this profile is accurate only in the low-density region measured by the 4ω probe and is expected to strongly diverge from the actual plasma profile closer to the driven shell.

The experimentally measured low-density plasma profiles were found to have expanded significantly farther than 1-D *LILAC* [8] (Fig. 3) and 2-D *DRACO* [9] radiation-hydrodynamic simulations predict. The laser drive in the 1-D *LILAC* code was properly reduced to account for corona deformation and lateral thermal conduction and radiation losses. At the earliest measured time (1 ns), the low-density plasma is 40 μm in front of the predictions, while the position of the shell is in good agreement. Between 1 ns and 4 ns the low-density plasma (at 10^{20} cm^{-3}) travels at an average velocity of ~205 μm/ns while its scale length expanded from 10 μm to 63 μm. The average simulated expansion speed of 145 μm/ns at 10^{20} cm^{-3} was slower than the measurements, and the scale lengths increased from 2 μm to 15 μm, which are shorter than measured across the entire time span. This discrepancy was largely insensitive to the thermal transport and the EOS models used in the simulations.

It was found in simulations that the position of the low density plasma, as well as its scale length, significantly depend on the mass density profile at the rear surface of the CH shell right before the shock breaks out. Figure 4 compares the measured density trajectory with simu-

lation results that varied the rear surface profile prior to the shock breakout. The simulation results shown in Fig. 3, as well as the 10^{19} cm^{-3} and 10^{20} cm^{-3} trajecotries shown in Fig. 4 (dashed lines), used an infinitely sharp boundary on the rear side of the CH, as is typical in hydrodynamic simulations. These simulations significantly underestimate the plasma expansion at all times. When the rear side of the CH target was relaxed over 10 μm (linear increase from zero to solid density) prior to the shock breakout, the simulated trajectories are in excellent agreement with the measurements (Fig. 4). The increased heating (from 20 eV to ~100 eV) that occurs from the shock propagating through the relaxed rear side of the shell, results in a faster expansion and larger scale length than when the shock breaks out of the standard sharp interface. Note the trajectory of the shell was unchanged by this relaxation.

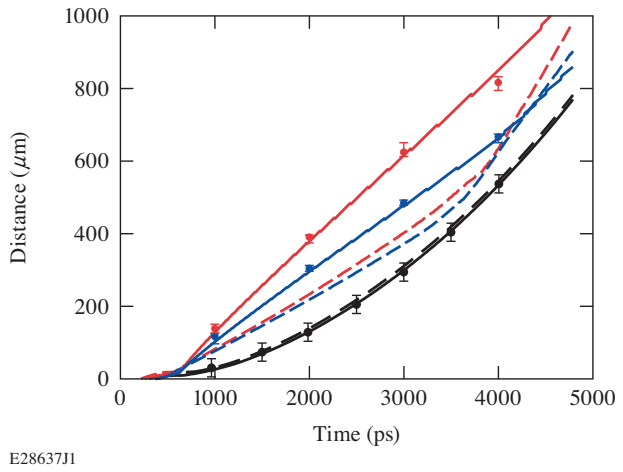

FIG. 4: The measured (black points) and simulated (black curves) shell trajectories. The measured (points) and simulated (curves) plasma density trajectories at 10^{19} cm^{-3} (red) and 10^{20} cm^{-3} (blue). The dashed lines are from simulations with no CH relaxation and the solid lines are from simulations initiated with 10 μm of expansion on the rear side of the CH shell.

An estimate of radiation preheat by coronal x-rays suggests a density gradient of ~4 μm, consistent with the simulations. The *LILAC* simulations (using Astrophysical opacity tables [10]) predict that 10 kJ/cm^3 is absorbed by a unit volume of solid CH on the rear surface during the shock transit time. This energy will heat the CH shell to ~0.5 eV. Considering the boiling temperature of CH, ~0.42 eV [11], it is reasonable to assume the CH polymer will sublime into vacuum forming the density gradient. The width of the gradient was estimated as four times the speed of sound in CH gas (~3500 m/s) times ~1/2 of the shock transit time of 600 ps. This early expansion of the CH shell cannot be expected to be modeled correctly in LILAC or DRACO because the hydrodynamic equations do not simulate the melting, evaporation, and expansion of a polymer.

Figure 5 shows the effects of an expanded inner surface of direct-drive ICF implosions, where an inner gradient consistent with these measurements suggests a reduced convergence leading to a 18% lower areal density and a 17% smaller ion temperature. Just after the shock breaks out (~1.1 ns), the inner surface of the simulations that included enhanced inner gradients began to grow (Fig. 5). These simulations used a spherical shell of 900 μm diameter outer surface, with a 8.4 μm CH ablator and 53 μm DT ice layer. The target was driven by a triple picket laser pulse with an on target drive intensity of 9×10^{14} W/cm^2 [12]. To increase the expansion rate of the material released on the inner shell consistent with the measurements reported here, 10 J was deposited on the inner 10 μg of the DT ice between the third picket and the main drive. This additional material on the inner surface reduced the compressibility of the hot spot increasing its radius at stagnation from 24.7 μm to 26.1 μm (6%) and decreasing the ion temperature from 3.17 keV to 2.64 keV. The resulting areal density decreased from 179 mg/cm^2 to 146 mg/cm^2 and the neutron yield decreased by more than a factor of 2 (8.1 to 3.8×10^{13} neutrons).

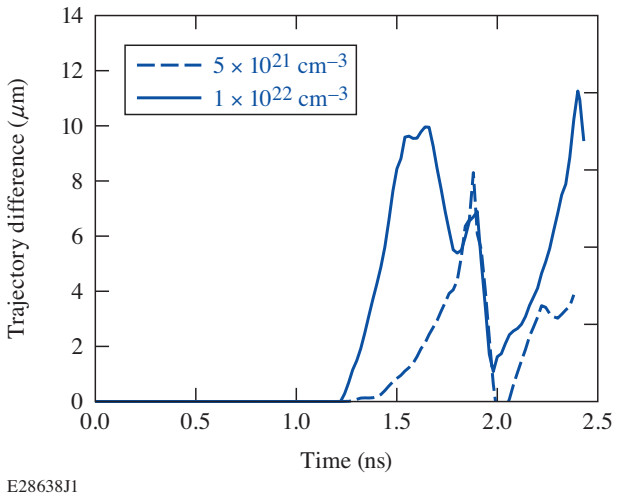

FIG. 5: The difference between inner shell trajectories with and without the enhanced inner surface is plotted for density contours of 5×10^{21} cm^{-3} (dashed) and 10^{22} cm^{-3} (solid).

In summary, optical probing using interferometry and angular filter refractometry was used to study the material release from the shock breakout at conditions relevant to ICF implosions. It was observed that the position and scale length in the measured density range (10^{19} to 10^{20} cm^{-3}) of the rarefaction wave strongly depend on the density profile at the rear surface of the CH before the shock breaks out. To match the experimental data, simulations required an initial material density gradient on the rear surface of the CH shell before the shock breaks out. This lower-density material is strongly heated by the

passing shock that causes it to expand more rapidly and have a longer scale length at later times. Radiation preheat by coronal x-rays can cause such a relaxation of the rear surface of the CH and formation of the density gradient. Simulations of direct drive cryogenic implosions that enhanced the inner surface release consistent with these measurements show a significant reduction in target performance, including an 18% reduction in areal-density, 17% reduction in ion temperature, and more than a factor of 2 reduction in the neutron yield.

This material is based upon work supported by the Department of Energy National Nuclear Security Administration under Award Number DE-NA0003856, the University of Rochester, and the New York State Energy Research and Development Authority.

* Electronic address: dhab@lle.rochester.edu

[1] D.S. Clark, C.R. Weber, A.L. Kritcher, J.L. Milovich, P.K. Patel, S.W. Haan, B.A. Hammel, J.M. Koning, M.M. Marinak, M.V. Patel, C.R. Schroeder, S.M. Sepke and M.J. Edwards, Nucl. Fusion **59**, 032008 (2019).

[2] S. Le Pape, L.F. Berzak Hopkins, L. Divol, A. Pak, E.L. Dewald, S. Bhandarkar, L.R. Bennedetti, T. Bunn, J. Biener, J. Crippen, D. Casey, D. Edgell, D.N. Fittinghoff, M. Gatu-Johnson, C. Goyon, S. Haan, R. Hatarik, M. Havre, D. D-M. Ho, N. Izumi, J. Jaquez, S.F. Khan, G.A. Kyrala, T. Ma, A.J. Mackinnon, A.G. MacPhee, B.J. MacGowan, N.B. Meezan, J. Milovich, M. Millot, P. Michel, S.R. Nagel, A. Nikroo, P. Patel, J. Ralph, J.S. Ross, N.G. Rice, D. Strozzi, M. Stadermann, P. Volegov, C. Yeamans, C. Weber, C. Wild, D. Callahan, and O.A. Hurricane, Phys. Rev. Lett. **120**, 245003 (2012).

[3] D. T. Michel, C. Sorce, R. Epstein, N. Whiting, I. V. Igumenshchev, R. Jungquist, and D. H. Froula, Rev. Sci. Instrum. **83**, 10E530 (2012).

[4] M. A. Barrios, D. G. Hicks, T. R. Boehly, D. E. Fratanduono, J. H. Eggert, P. M. Celliers, G. W. Collins, and D. Meyerhofer, Phys. Plasmas **17**, 056307 (2010).

[5] J.H. Kelly, L.J. Waxer, V. Bagnoud, I.A. Begishev, J. Bromage, B.E. Kruschwitz, T.J. Kessler, S.J. Loucks, D.N. Maywar, R.L. McCrory, D.D. Meyerhofer, S.F.B. Morse, J.B. Oliver, A.L. Rigatti, A.W. Schmid, C. Stoeckl, S. Dalton, L. Folnsbee, M.J. Guardalben, R. Jungquist, J. Puth, M.J. Shoup III, D. Weiner and J.D. Zuegel, J. Phys. IV France **133**, 75 (2006).

[6] A. Howard, D. Haberberger, R. Boni, R. Brown, and D. H. Froula, Rev. Sci. Instrum. **89**, 10B107 (2018).

[7] D. Haberberger, S. Ivancic, S. X. Hu, R. Boni, M. Barczys, R. S. Craxton, and D. H. Froula, Phys. Plasmas **21**, 056304 (2014).

[8] J, Delettrez, R. Epstein, M. C. Richardson, P. A. Jaanimagi, and B. L. Henke, Phys. Rev. A **36**, 3926 (1987).

[9] P. B. Radha, V. N. Goncharov, T. J. B. Collins, J. A. Delettrez, Y. Elbaz, V. Yu. Glebov, R. L. Keck, D. E. Keller, J. P. Knauer, J. A. Marozas, F. J. Marshall, P. W. McKenty, D. D. Meyerhofer, S. P. Regan, T. C. Sangster, D. Shvarts, S. Skupsky, Y. Srebro, R. P. J. Town, and C. Stoeckl, Phys. Plasmas **12**, 032702 (2005).

[10] W. F. Huebner, A. L. Merts, N. H. Magee, Jr., and M. F. Argo, Los Alamos National Laboratory, Los Alamos, NM, Report No. LA-6760-M, 1977 (unpublished)

[11] J.G. Speight, Lange's Handbook of Chemistry, 16th edition, p. 1.124, McGraw-Hill Education: New York, Chicago, San Francisco, Lisbon, London, Madrid, Mexico City, Milan, New Delhi, San Juan, Seoul, Singapore, Sydney, Toronto, (2005)

[12] V. N. Goncharov, T. C. Sangster, T. R. Boehly, S. X. Hu, I. V. Igumenshchev, F. J. Marshall, R. L. McCrory, D. D. Meyerhofer, P. B. Radha, W. Seka, S. Skupsky, C. Stoeckl, D. T Casey, J. A. Frenje, and R. D. Petrasso, Phys. Rev. Lett. **104**, 165001 (2010).